Sixth International Symposium on Marine Propulsors
smp'19, Rome, Italy, May 2019

Pattern Recognition in Hydroacoustic Cavitation Measurements

Christian Krueger[1], **Sascha Spors**[1], **Andreas Wolter**[2]

[1]Institute of Communications Engineering, University of Rostock, Rostock, Germany
[2]Institute of Fluid Mechanics, University of Rostock, Rostock, Germany

ABSTRACT

Hydro-acoustics play a major role in modern propeller design, as shipbuilders are facing new regulations for underwater noise emissions of merchant ships. In this paper a method for analyzing and clustering audio data from hydro-acoustic cavitation measurements is presented. The measurements were performed with beamforming methods in a cavitation tunnel and with a single hydrophone for a frequency range between 22Hz and 104kHz. For extraction of the cavitation noise, the measurement data was filtered with the Teager-Kaiser Energy operator (TKE). Using a wavelet decomposition for a dimension reduction of the audio data, the wavelets can be clustered with a k-Means algorithm. The results suggest that cavitation regions with different acoustic features exist. Based on the underlying assumption that individual cavitation events are segmented by non cavitating classes, the analysis reveals frequent cavitation patterns as well as their individual pattern elements. This gives a detailed insight into the nature of cavitation and may allow for an estimation of individual cavitation types for certain propeller operation points.

Keywords

propeller, cavitation, acoustics, beamforming

1 INTRODUCTION

With upcoming regulations, restricting the underwater noise emission of merchant ships, reliable methods for cavitation monitoring are of increasing interest. The acoustic contribution of individual cavitation types is widely measured and documented (Carlton 2018). However, as acoustic emissions arise already from smallest cavitation bubbles, optical observations in model tests are not suitable for acoustic propeller evaluation. This leads to a strong demand for identification methods that deliver detailed information about cavitation type, inception, area and intensity.

2 METHOD

2.1 Filtering

The presented method is a combination of different audio filtering and processing routines that are easy to implement in a post-processing chain. Cavitation noise can be divided in discrete, broadband and combined characteristics that superimpose from all types of emerging, pulsating, collapsing and rebounding bubbles, sheets and vortices. In the simplest case a cavitation bubble produces a high energy pressure signal, that is characterized by a steep increase followed by a moderate fall (Vogel et al. 1989). To capture this effect, a filter is needed that extracts the specific transient. The Teager-Kaiser Energy operator (TKE) presented by Kaiser (1990) in continuous domain reads

$$\begin{aligned}\Psi\left[x(t)\right] &= \left(\frac{dx(t)}{dt}\right)^2 - x(t)\frac{d^2x(t)}{dt^2} \\ &= \dot{x}^2 - x\ddot{x}\end{aligned} \tag{1}$$

with the signal x, and its first and second time derivative $\dot{x}$ and $\ddot{x}$ respectively. For the discrete measurement signal the TKE operator can be written as

$$\Psi\left\{x\left[n\right]\right\} = x^2\left[n\right] - x\left[n-1\right]x\left[n+1\right] \tag{2}$$

The TKE operator extracts a measure of the energy produced by a mechanical process. Although the frequency information is corrupted due to the nonlinear term, individual characteristics of the cavitation events can be found in the frequency domain. For dimension reduction of the filtered audio data, the algorithm proposed by Mallet (1989) with a 3rd order Daubechies wavelet was used. As different cavitation types show individual contribution to different regions within the frequency spectra, the wavelet vector presents our feature set for the machine learning algorithm. In this approach an unsupervised k-Means algorithm (Hartigan and Wong, 1979) was applied to identify signal elements with specific characteristics. In general, supervised models deliver better results. However, in most cases annotated datasets do not exist for a given propeller configuration.

2.2 Beamforming

For localization of the spatial distributed acoustic sources a delay-and-sum beamforming approach was applied. The measurement signals were split into blocks of length $L = 2^n$ with an overlap of $O = 0.5L$, windowed with a Hanning window. The cross-spectral matrix (CSM) is built from the averaged Fourier transforms. To reduce noise sources induced by the hydrophones themselves, the primary diagonal of the CSM, presenting the signals auto-correlation, was set to zero. The time delay Δt is computed from the known distances of each scan position with respect to the

*

hydrophone locations. For an acoustic source $\vec{x}_t$ the steering vector in frequency domain reads

$$g\left(\vec{x}_t, \omega_k\right) = \frac{1}{M}\left(e^{-i\omega_k \Delta t_0}, ..., e^{-i\omega_k \Delta t_{M-1}}\right)^T \quad (3)$$

for a number of hydrophones M. The acoustic map $b\left(\vec{x}_t, \omega_k\right)$ is defined as follows

$$b\left(\vec{x}_t, \omega_k\right) = g^T\left(\vec{x}_t, \omega_k\right) CSM\left(\omega_k\right) g\left(\vec{x}_t, \omega_k\right) \quad (4)$$

3 EXPERIMENTAL SETUP

The model scale experiments were carried out at the K-21 cavitation tunnel at the University of Rostock. The cavitation tunnel provides a rectangular cross section of $0.3\,m \times 0.3\,m$ and operates at pressures down to $p_{abs} = 0.4\,bar$ with a turbulence intensity of $T_u = 1.5\%$ for velocities up to $v_i = 9.5\,m/s$. For the cavitation test a semi-detached swept wing with an aspect ratio of $\Lambda = 4.0$, a span of $b = 0.15\,m$ and a root chord length of $C = 0.063\,m$ was installed. The foil geometry blends from four 4-digit NACA profiles and provides a theoretical lift coefficient of $c_L = 0.073\,\alpha$. To ensure a pronounced cavitating tip vortex with defined detachment point, the wing was designed with increased tip loading. The generator line is positioned parallel to the y-axis with its basis at $P_{GA} = [0.0538\ 0.150\ 0]\,m$. A detailed listing of the foil geometry can be found in Table 1.

Table 1: Foil geometry

y/b	NACA	c $[m]$	α $[\circ]$
0	8518	0.0630	8
0.5	7516	0.0563	10
0.74	0012	0.0420	12
1	0010	0.0375	16

The cavitation measurement consists of a series of velocity ramps, starting with an inlet velocity of $v_i = 2.0\,m/s$, increasing the velocity linearly for $t = 150\,s$ up to $v_i = 7.0\,m/s$ followed by a linear decrease for $t = 150\,s$ back to $v_i = 2.0\,m/s$. The relative channel pressure of $p_c = -40\,kPa$ results in cavitation numbers ranging between $2.42 < \sigma < 29.7$ at the tip of the hydrofoil. The acoustic array consists of 16 hydrophones of type BKSV 8103, combining a beamforming and a former time-difference of arrival (TDOA) pattern. The hydrophones were flush-mounted into the side (12 hydrophones) and the lower channel windows (4 hydrophones), facing the suction side and the tip of the foil (Fig.1). With a synchronized sample rate of $f_s = 262\,kHz$ the acoustic field was measured up to a frequency of $f \leq 102.4\,kHz$.

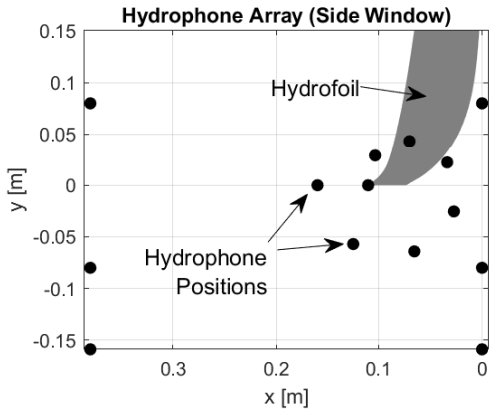

Figure 1: Hydrophone array: Location of the hydrophones acoustic centers (black dots) related to the hydrofoils position (gray)

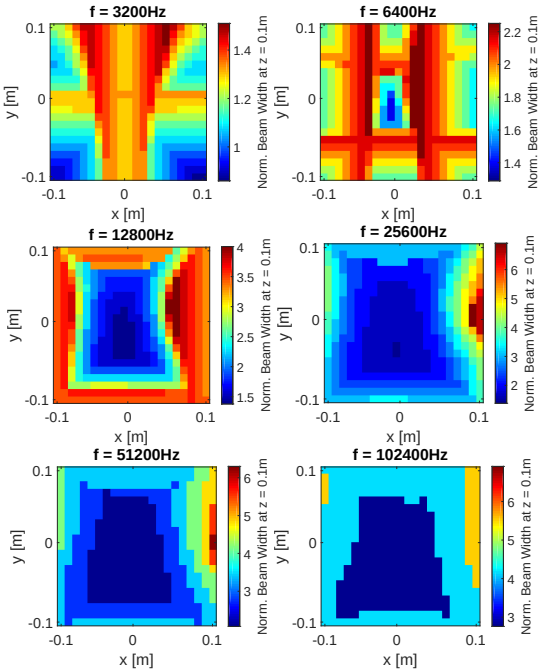

Figure 2: Calculated normalized beam lobe width for the combined hydrophone array for different frequencies for focus points at $z = 0.1\,m$

Combining the given TDOA and a beamforming array significantly reduces the degree of freedom for hydrophone positioning. While the TDOA array delivers precise results enclosing the noise sources, the beamforming pattern needs to be designed with respect to the expected frequency range, as the signal attenuation gets minimal when the relation of wavelength and hydrophone inter-distance meets $\lambda/d_h = 2$. The array consists of 16 hydrophones only, which is split in 8 hydrophones for the TDOA pattern and 8 hydrophones for the beamforming pattern. The hydrophone positions were calculated for a Archimedean spiral and a Underbrink configuration using the algorithm of Prime and Doolan (2013). For this comparably small beamforming array a spiral type with 2π, an inner diameter of $D_i = 0.03\,m$ and an outer diameter of $D_o = 0.08\,m$

presented the best results for the normalized beam lobe width (Fig. 2).

4 RESULTS

The cavitation tunnel experiments ranged over different cavitation types: Starting with a cavitation-free operation point at the blade, the tip vortex already showed enclosed gas bubbles at the very beginning of the experiment. It can be expected, that the initial bubbles hold dissolved air only. With increasing velocity, a clearly detached solid bubble is formed within the vortex core, starting to stretch upstream to the foils tip. At an inlet velocity of $v_i = 4.8\,m/s$ ($\sigma = 5.15$) the cavitating bubble within the tip vortex attaches to the tip, initializing stable suction side sheet cavitation at $r/R \geq 0.8$ and $c_x/c \leq 0.2$. Increasing the velocity further, the suction side sheet cavitation bubble grows in span and chord direction, reaching its full cavitation extension at $v_i = 7.0\,m/s$ over the whole span for chord lengths of $c_x/c \leq 0.65$. In contrast to the upwards velocity ramp, in the downwards ramp the sheet cavitation quickly reduces back to its former tip location at $r/R \geq 0.8$, showing strong chordwise pulsation over a wide velocity range with repeatedly detachment of the cavitating tip vortex bubble. Different cavitation states are shown in Fig. 3.

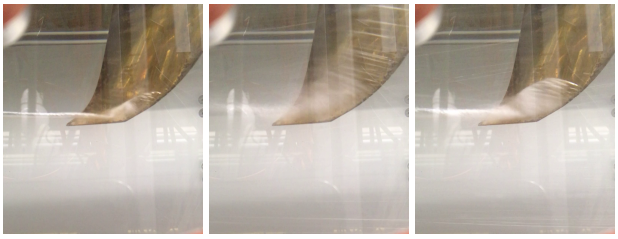

Figure 3: Cavitation states from the tunnel experiments: Attachment of the cavitating tip vortex and inception of suction side sheet cavitation at velocity increase (left); stable sheet cavitation in maximum extent at velocity peak (center); pulsating sheet cavitation with reattaching tip vortex cavitation during decreasing velocity (right)

For identification of the cavitation type, in most cases the location of the cavitation bubble is a strong indication. Therefore the noise emitting areas on the propeller are of special interest. In typical acoustic camera applications, the beamforming algorithm scans over a plane parallel to the beamforming array. As the propeller geometry and position in most cases is known a priori, it can be used as the steering vector for the beamforming algorithm. For the given configuration the acoustic intensity map for discrete frequencies shows a good agreement with the observed cavitation extension (Fig. 4).

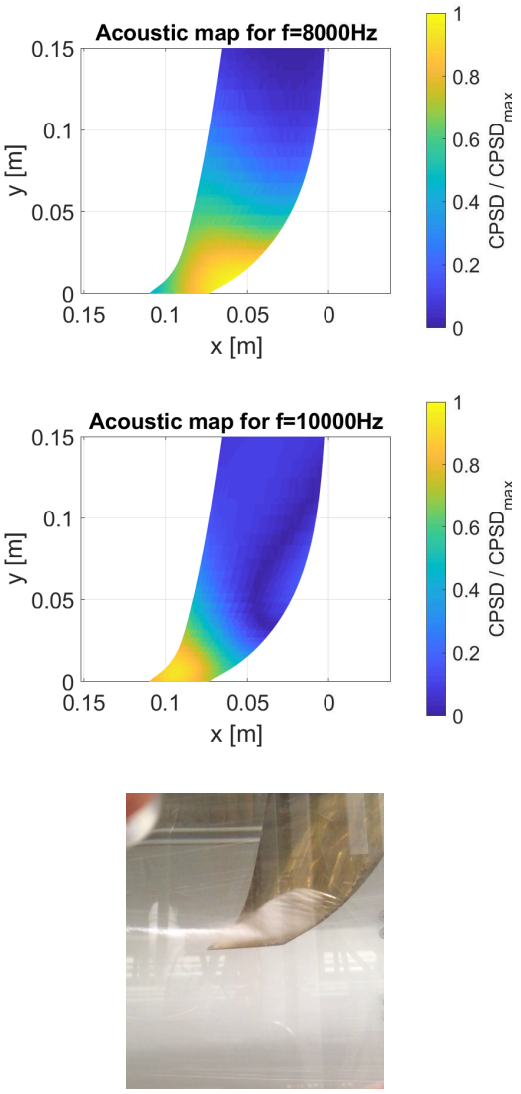

Figure 4: Acoustic maps at $8kHz$ (top) and $10kHz$ (center) for the pulsating cavitation state (bottom)

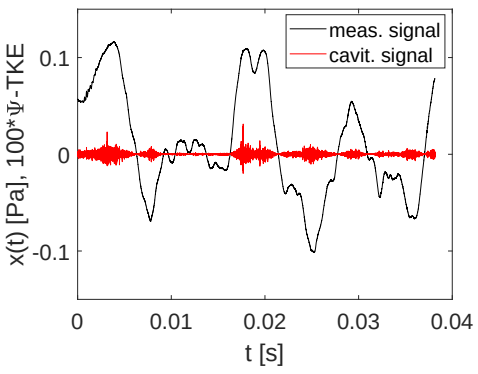

Figure 5: Audio signal from the delay-and-sum beamformer (black) and extracted TKE cavitation signal (red)

When the position of the cavitation region is calculated, the delay-and-sum signal of an arbitrary steering point within the cavitating area can be used for further analysis. Firstly

the data is filtered with the TKE operator to extract the cavitation signal from the background noise (Fig. 5). Using the wavelet decomposition, the cavitation signal is dimensionally reduced (Fig. 6).

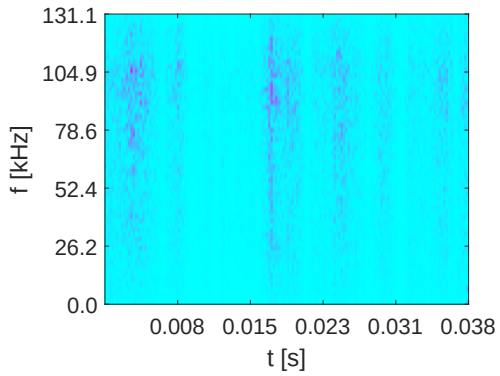

Figure 6: Wavelet decomposition of the extracted TKE cavitation signal

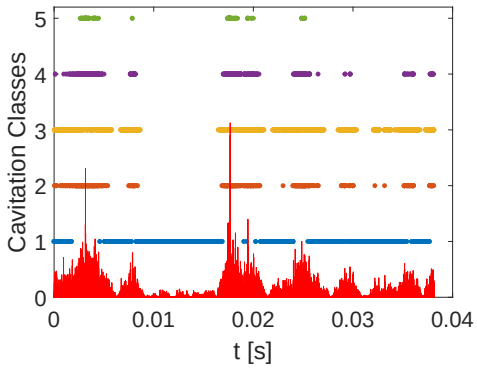

Figure 7: Calculated cavitation classes from the k-Means algorithm

Classifying the wavelet vectors with the k-Means algorithm results in different cavitation classes for the considered cavitation region (Fig. 7). In this example a cluster number of $k = 5$ was selected, to present a clear differentiation between signal elements. Increasing cluster numbers result in a more detailed segmentation of the audio data. As the presentation in Fig. 7 is fairly dense, one has to point out, that every time instance of the cavitation signal is assigned to one single cavitation class only. These classes represent groups of signal elements with similarities in frequency space, but do not necessarily relate to certain cavitation types. Although it can be expected, that a sufficient large number of cavitation classes allows for individual cavitation type separation, supervised classification algorithms are more suitable in this case. Unfortunately, their application requires a large database of annotated data, that in most cases does not exist. Looking closely at the class distribution in Fig. 7, the times $0.01\,s < t < 0.02\,s$ are dominated by cavitation class one. Comparing the distribution with the TKE signal, it can be seen, that this specific section relates to a low-level cavitation signal. Keeping in mind, that the delay-and-sum signal is analyzed, this low-level region may contain cavitation events outside of the beamforming focus. Therefore cavitation class one may be the low-level threshold or cavitation-free region. Under the assumption, that sparse cavitation events are separated by cavitation-free sections, the signal can be calculated for typical cavitation class patterns or motifs. For a better signal-to-noise ratio, class one and three are used to represent the cavitation free regions in this example. Sorting the segmented cavitation patterns, it can be noticed, that single cavitation events of class two are most frequent within our short measurement signal for the focused cavitation region, followed by combinations of class two and four (Fig. 8). Comparing cavitation patterns as well as their distribution for different cavitation areas may be suitable as a starting point for detailed investigation of different cavitation types.

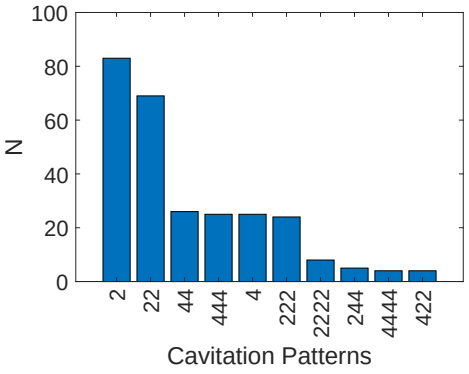

Figure 8: Most frequent cavitation patterns of the pulsating suction side sheet cavitation

CONCLUSION

In this paper a method for pattern recognition in acoustic cavitation measurements was presented. It was shown, that cavitation areas can be localized and identified acoustically. Using the TKE operator, the cavitation signal can be extracted from the background noise. With the combined audio signal of the delay-and-sum beamformer, the individual analysis of defined cavitation regions is possible. A clustering algorithm was used with a wavelet decomposition featureset to group cavitation elements with similarities in frequency space. Typical cavitation patterns were identified.

A known weak spot of the method relates to the unsupervised k-Mean algorithm, as the cavitation classes are relative and built randomly. Supervised algorithms, based on annotated data, may deliver better results for reliable identification of individual, mixed or interacting cavitation types, but require annotated datasets. As combined measurements for acoustical and optical cavitation localization and tracking are planned in future works, an annotated database is built up, to provide application of supervised classification algorithms.

Although the case presented was far from being complex compared to a propulsion test case, our investigations

showed, that an even simpler case may be favorable for building up a solid audio database with only sparse cavitation events.

REFERENCES

Carlton, John. (2018). 'Marine propellers and propulsion'. Butterworth-Heinemann.

Hartigan, J. A., and M. A. Wong. (1979) 'Algorithm AS 136: A K-Means Clustering Algorithm.' Journal of the Royal Statistical Society. Series C (Applied Statistics), vol. 28, no. 1, pp. 100108. JSTOR, www.jstor.org/stable/2346830.

Kaiser, J. F. (1990, April). 'On a simple algorithm to calculate the'energy'of a signal'. In Acoustics, Speech, and Signal Processing. ICASSP-90. International Conference on (pp. 381-384). IEEE.

Mallat, S.G. (1989) 'A theory for multiresolution signal decomposition: The wavelet representation'. volume 11, pages 674-693. IEEE Transaction on Pattern Analysis and Machine Intelligence.

Prime, Zebb, and Con Doolan. (2013) 'A comparison of popular beamforming arrays'. Australian Acoustical Society AAS2013 Victor Harbor 1.

Vogel, A., Lauterborn, W., & Timm, R. (1989). 'Optical and acoustic investigations of the dynamics of laser-produced cavitation bubbles near a solid boundary'. Journal of Fluid Mechanics, 206, 299-338.